Research Article Vol. 33, No. 22 / 3 Nov 2025 / Optics Express 46224
Optics EXPRESS

Iterative wavelet-transform-based surface decomposition algorithm for multi-tool fabrication in computer-controlled optical surfacing

JIANJIE ZHOU,[1,2,3] BO LI,[1,2,*] XINNAN LI,[1,2] AND MINTAO ZHANG[1,2,3]

[1]Nanjing Institute of Astronomical Optics & Technology, Chinese Academy of Sciences, Nanjing 210042, China
[2]CAS Key Laboratory of Astronomical Optics & Technology, Nanjing Institute of Astronomical Optics & Technology, Nanjing 210042, China
[3]University of Chinese Academy of Sciences, Beijing 100049, China
[*]bli@niaot.ac.cn

Abstract: As demand for high-precision optical mirrors in astronomy increases, combined fabrication using multiple polishing tool sizes has been adopted widely. To address remaining limitations in computational and fabrication efficiency, this paper proposes an iterative wavelet-transform-based surface decomposition algorithm (IWTSD) and an associated multi-tool fabrication strategy. IWTSD applies the two-dimensional dual-tree complex wavelet transform (2D-DTCWT) with iterative refinement to decompose a target surface into two or more scale-separated, non-negative component surfaces. Specific surface extension operation with an optimized factor is used to adapt IWTSD for non-rectangular apertures. This decomposition reduces both computational cost and total polishing dwell time compared with similar methods. Simulations demonstrate that IWTSD-based multi-tool fabrication achieves comparable surface error convergence using only 2/3 of the dwell time required by other multi-tool fabrication based on alternative surface decomposition algorithms, and yields a residual RMS about 1/3 that of single-tool fabrication. Experimental polishing of a 1150 mm off-axis aspheric mirror showed that overall RMS decreased from 0.655 λ to 0.21 λ, and residuals at each scale were substantially reduced. These results demonstrate that the proposed method can improve fabrication efficiency for large-aperture optical mirrors with low computational cost.

1. Introduction

The demand for high-precision optical mirrors in advanced astronomy is steadily increasing [1,2]. For instance, primary mirrors for next-generation ground-based telescopes are reaching diameters in the class of 30 meters [3,4], while the number of off-axis segmented mirrors with apertures of 1.44 m can exceed 900. This scale of manufacturing poses dual challenges in both precision and efficiency. Computer-controlled optical surfacing (CCOS), a widely adopted and powerful manufacturing technology for aspheric and free-form optics, has been continuously refined over the past several decades [5–7]. However, improving fabrication efficiency remains a critical issue, as CCOS polishing tools are typically much smaller than mirror apertures, which limits material removal rates and prolongs manufacturing time.

In conventional CCOS processes, the dwell time for each polishing round is typically optimized for a single tool size. During the early manufacturing stages, large-scale surface errors dominate, so larger tools are used for correction [8]. In contrast, smaller tools are required to correct small-scale surface errors during later stages. Although strategies such as increasing tool size [9,10] and minimizing total dwell time [11] can improve single-tool fabrication efficiency, the corrective

#578980 https://doi.org/10.1364/OE.578980
Journal © 2025 Received 16 Sep 2025; revised 10 Oct 2025; accepted 13 Oct 2025; published 22 Oct 2025

Optics EXPRESS

capability of a single tool is limited to a specific spatial scale, making it suboptimal for the overall mirror fabrication process. By contrast, employing tools of multiple sizes—either concurrently or sequentially—within a single manufacturing round helps to reduce total dwell time and improve convergence efficiency across different spatial scales [8,12]. This improved convergence also reduces the number of required surface measurements, which are time-consuming due to workpiece handling, fixation, and the need for structural and environmental stabilization [13,14]. Consequently, a multi-tool combined fabrication strategy can substantially shorten the overall mirror fabrication cycle.

Two classes of methods are currently used for combined fabrication using multiple polishing tool sizes. One class simultaneously optimizes the dwell time maps of multiple tools using a single surface error map. For example, in 2009, Kim et al. proposed a non-sequential multi-tool optimization based on a linear equations model, using a gradient search method to compute the dwell time maps for all tools in one optimization step [8]. This approach improved convergence and reduced the mid-spatial-frequency residuals. In 2022, Kang et al. extended Kim's model with a genetic-algorithm-powered, non-sequential dwell time optimization method, enhancing computational efficiency, smoothing the dwell time map, and improving its similarity to the target removal map [15]. In the same year, Ke et al. proposed a multi-tool dwell time optimization that accounts for CNC dynamics, solving a Tikhonov regularized linear system via an iterative least-squares solver with MR (LSMR) factorization to compute the dwell times [16]. These methods balanced tool runtimes and produced smooth dwell time distributions. However, these linear equations model-based approaches construct a removal coefficient matrix by incorporating multiple tool influence functions (TIFs), which enlarges the coefficient matrix, imposes a substantial computational burden, and complicates iterative optimization. Consequently, computation times can extend to several hours, severely limiting the practical engineering application.

The second class of methods decomposes a surface error map into scale-specific components using techniques such as Zernike polynomial fitting [17–19], frequency filtering [20–22], or two-dimensional discrete wavelet transform (2D-DWT) [23]. Tools of different sizes are then assigned to each component, and the dwell times are calculated separately for each scale, allowing for concurrent correction of surface errors during a single fabrication round. In 2017, Liu et al. proposed a multi-tool fabrication method based on surface error decomposition, using the first 36 Zernike terms to fit a low-order error map [17]. The residual error, obtained by subtracting the simulated removal of the low-order error map from the original surface error map, served as the high-order error map. Relatively larger tools were used to correct the low-order errors, while smaller tools were used to correct the high-order errors, enabling the successful fabrication of a 4 m SiC aspheric mirror [18,19]. In 2020, Du et al. introduced a frequency filtering approach to decompose the surface, correct the low-frequency errors, and smooth mid-to-high spatial frequency errors, thereby accelerating the improvement of surface accuracy [20]. Similarly, Xu et al. and Zhong et al. proposed frequency-filtering-based surface decomposition and multi-tool fabrication schemes to improve precision and efficiency in continuous-phase-plate manufacturing [21,22]. However, the mid-to-high spatial frequency components obtained by these surface decomposition algorithms are not guaranteed to be non-negative, which makes them unsuitable for direct dwell time calculation. Enforcing non-negativity by subtracting the component's minimum value produces a positive component. But it will result in a significantly increased fabrication time, which contradicts the goal of improving fabrication efficiency.

To address the high computational cost of class-one methods and the long fabrication time of class-two methods, we propose an iterative wavelet-transform-based surface decomposition algorithm (IWTSD) and an associated multi-tool fabrication strategy to improve both computational and fabrication efficiency. Firstly, IWTSD employs the dual-tree complex wavelet transform for its approximate shift invariance and improved directional selectivity. Secondly, an iterative

Optics EXPRESS

refinement procedure is proposed to ensure the non-negativity of each scale-separated component surface without a positive bias operation. Thirdly, a specific surface extension method and an optimized extension factor are introduced to ensure the decomposition of non-rectangular surfaces and adjust the ratio of edge surface decomposition across scales. Finally, dwell times are then computed independently for each scale, enabling concurrent correction of surface errors across all scales and thus quicker convergence of the overall surface error in the full aperture within a single fabrication round. IWTSD-based multi-tool fabrication reduces surface decomposition and dwell time calculations to under 10 s on a standard personal computer and reduces total polishing dwell time by over 30% relative to similar decomposition-based approaches, combining the low computational cost of the decomposition-based methods with the dwell-time-saving benefits of direct multi-tool optimization.

In this paper, Section 2 presents the theory of the iterative wavelet-transform-based surface decomposition algorithm. Section 3 details the IWTSD-based multi-tool fabrication method and demonstrates its advantages over traditional approaches, such as single-tool fabrication and other multi-tool methods using alternative surface decomposition algorithms. Section 4 describes experiments that validate the feasibility and reliability of the proposed method. Finally, Section 5 concludes the paper and presents the directions for future work.

2. Theory and algorithm

As manufacturing progresses, errors with multiple spatial scales appear and can be broadly categorized into (1) large-scale shape errors and (2) small-scale fragmented or annular errors. For multi-tool fabrication, it is therefore essential to decompose the surface error by scale and to generate non-negative component surfaces that are suitable for dwell time calculation.

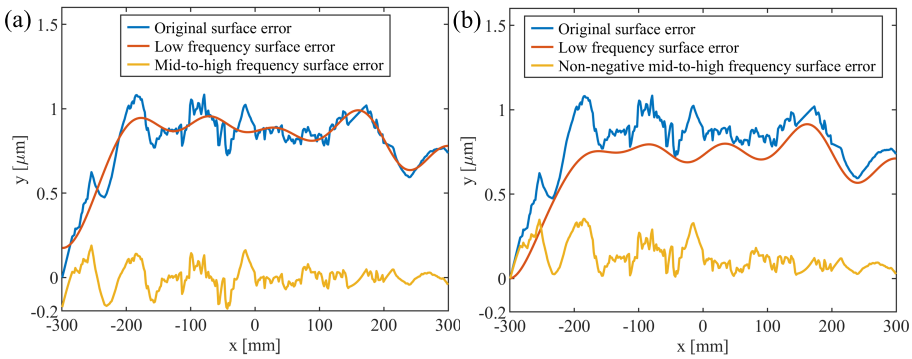

Fig. 1. (a) Decomposition of a representative one-dimensional surface profile using frequency filtering; (b) Ideal surface decomposition.

Frequency-filtering methods—most commonly based on the Fourier transform—decompose a surface error map using infinite, periodic sine and cosine basis functions [20–22]. Because the surface error map is a non-stationary signal with localized features, the Fourier transform cannot simultaneously localize spatial and frequency information, and thus represents local error characteristics poorly [24]. In addition, frequency filtering does not directly generate two non-negative component surfaces. Figure 1(a) illustrates a Fourier-based decomposition of a representative one-dimensional surface profile: the low-frequency component captures the overall contour, while the mid-to-high frequency component captures small-scale errors. In this example, the mid-to-high frequency component contains negative values. In practice, the surface must be non-negative for dwell time calculation, and a common operation—subtracting its minimum to enforce non-negativity—introduces a positive bias, which will increase total material removal and thus fabrication time. Ideally, the low-frequency component retains large-scale errors without

Optics EXPRESS

exceeding the original surface value, and the mid-to-high frequency component represents small-scale errors and is non-negative, as shown in Fig. 1(b). To satisfy these requirements, we propose an iterative wavelet-transform-based surface decomposition algorithm.

2.1. Surface decomposition based on two-dimensional dual-tree complex wavelet transform

Unlike the Fourier transform, the wavelet transform uses finite, decaying basis functions rather than infinite trigonometric bases, improving frequency resolution at low frequencies while providing better spatial localization at high frequencies. However, the commonly used 2D-DWT has two main limitations: (1) lack of shift invariance — identical features shifted in space can produce different decompositions, so small measurement-induced shifts cause large output variations; and (2) limited directional selectivity — diagonal and oriented features are poorly represented, often producing spurious ripple artifacts in reconstructed multi-scale surfaces. These limitations therefore undermine the reliability and precision of mirror fabrication.

Given the characteristics of mirror surface error maps, we adopt the dual-tree complex wavelet transform (DTCWT), originally proposed by Kingsbury [25–27], which has not previously been applied to mirror surface error analysis as far as we know. The DTCWT implements decomposition and reconstruction via two parallel DWT trees, each using a different filter set that satisfies the perfect reconstruction condition. By introducing limited redundancy (4:1 for two-dimensional signals), DTCWT achieves approximate shift invariance and improved directional selectivity, making it well-suited for the decomposition and reconstruction of mirror surface error maps.

2.1.1. Framework of DTCWT

In wavelet theory, any finite-energy signal $f(x)$ can be decomposed using scaling and wavelet functions as follows:

$$\begin{cases} f(x) = \sum_k c_{j_0}(k)\varphi_{j_0,k}(x) + \sum_{j=j_0}^{\infty}\sum_k d_j(k)\psi_{j,k}(x) \\ \varphi_{j,k}(x) = 2^{\frac{j}{2}}\varphi(2^j x - k) \\ \psi_{j,k}(x) = 2^{\frac{j}{2}}\psi(2^j x - k) \end{cases} \tag{1}$$

where $\varphi_{j,k}(x)$ and $\psi_{j,k}(x)$ denotes the scaling and wavelet functions. The integer k determines the translation of $\varphi_{j,k}(x)$ and $\psi_{j,k}(x)$ along the x-axis, while the integer j determines the width and amplitude of them. The approximation coefficient c_{j_0} and the detail coefficients d_j are obtained by the inner products:

$$\begin{cases} c_{j_0}(k) = \langle f(x), \varphi_{j_0,k}(x)\rangle = \int_{-\infty}^{\infty} f(x)\varphi_{j_0,k}(x)dx \\ d_j(k) = \langle f(x), \psi_{j,k}(x)\rangle = \int_{-\infty}^{\infty} f(x)\psi_{j,k}(x)dx \end{cases} \tag{2}$$

where $\langle\cdot,\cdot\rangle$ denotes the inner product operator.

In the DTCWT, the complex wavelet can be written as

$$\psi^{\mathrm{C}}_{j,k}(x) = \psi^{\mathrm{Re}}_{j,k}(x) + i\psi^{\mathrm{Im}}_{j,k}(x) \tag{3}$$

where $\psi^{\mathrm{Re}}_{j,k}(x)$ and $\psi^{\mathrm{Im}}_{j,k}(x)$ are wavelets of the two parallel trees, and $i = \sqrt{-1}$.

Correspondingly, the analysis yields two sets of coefficients:

$$\begin{cases} c^{\mathrm{Re}}_{j_0}(k) = \langle f(x), \varphi^{\mathrm{Re}}_{j_0,k}(x)\rangle \\ d^{\mathrm{Re}}_{j}(k) = \langle f(x), \psi^{\mathrm{Re}}_{j,k}(x)\rangle \end{cases}, \begin{cases} c^{\mathrm{Im}}_{j_0}(k) = \langle f(x), \varphi^{\mathrm{Im}}_{j_0,k}(x)\rangle \\ d^{\mathrm{Im}}_{j}(k) = \langle f(x), \psi^{\mathrm{Im}}_{j,k}(x)\rangle \end{cases} \tag{4}$$

Individual approximation or detail signals may be reconstructed by retaining only the corresponding coefficients from both trees. In the classical DTCWT reconstruction, the real-valued

Optics EXPRESS

approximation $c_{j_0}(x)$ or a single detail $d_j(x)$ is obtained by

$$\begin{cases} c_{j_0}(x) = \frac{1}{2}\left[\sum_k c_{j_0}^{\mathrm{Re}}(k)\varphi_{j_0,k}^{\mathrm{Re}}(x) + \sum_k c_{j_0}^{\mathrm{Im}}(k)\varphi_{j_0,k}^{\mathrm{Im}}(x)\right] \\ d_j(x) = \frac{1}{2}\left[\sum_k d_j^{\mathrm{Re}}(k)\psi_{j,k}^{\mathrm{Re}}(x) + \sum_k d_j^{\mathrm{Im}}(k)\psi_{j,k}^{\mathrm{Im}}(x)\right] \end{cases} \tag{5}$$

The reconstructed signals $c_{j_0}(x)$ and $d_j(x)$ are real-valued with the same sampling length as the original signal $f(x)$. In discrete implementations, one typically choose $j_0 = 0$, and $j = 0, 1, \ldots, J-1$, where J is the number of decomposition levels.

2.1.2. Directional bandpass subbands of 2D-DTCWT

For a separable (row-column) implementation, the 2D wavelet is written as

$$\psi(x, y) = \psi(x)\psi(y) \tag{6}$$

where the complex wavelet $\psi(x)$ is given by

$$\psi(x) = \psi^{\mathrm{Re}}(x) + i\psi^{\mathrm{Im}}(x) \tag{7}$$

Hence, $\psi(x, y) = \psi(x)\psi(y)$ can be expressed by

$$\begin{aligned} \psi(x, y) &= [\psi^{\mathrm{Re}}(x) + i\psi^{\mathrm{Im}}(x)][\psi^{\mathrm{Re}}(y) + i\psi^{\mathrm{Im}}(y)] \\ &= \psi^{\mathrm{Re}}(x)\psi^{\mathrm{Re}}(y) - \psi^{\mathrm{Im}}(x)\psi^{\mathrm{Im}}(y) + i[\psi^{\mathrm{Re}}(x)\psi^{\mathrm{Im}}(y) + \psi^{\mathrm{Re}}(y)\psi^{\mathrm{Im}}(x)] \end{aligned} \tag{8}$$

Consequently, the 2D-DTCWT produces six directional bandpass subbands at ±15°, ±45°, and ±75°. By contrast, the 2D-DWT only has horizontal and vertical orientations, which limits its ability to represent arbitrarily oriented, localized features. The additional directional subbands of the 2D-DTCWT substantially reduce aliasing artifacts and edge distortions when decomposing surfaces with numerous directional features. Reconstructed multi-scale surfaces are therefore smoother and exhibit improved rotational invariance compared with 2D-DWT reconstructions.

Despite these advantages, the direct application of 2D-DTCWT to mirror surface error maps has two practical shortcomings: (1) decomposition results are not, in general, non-negative and thus are not directly suitable for dwell time calculation; and (2) the standard 2D-DTCWT assumes data on rectangular grids and cannot handle non-rectangular apertures. To address these issues, we introduce the iterative refinement procedure and specialized surface extension methods (detailed in Sections 2.2 and 2.3, respectively), and then the comprehensive surface decomposition algorithm suitable for practical mirror surface analysis is obtained.

2.2. Non-negative surface decomposition based on iterative refinement

This paper proposes an iterative wavelet-transform-based surface decomposition algorithm that decomposes the target surface into at least two non-negative, scale-specific component surfaces and a decomposed residual. The algorithm iteratively extracts non-negative detail components from the current surface in the iteration and accumulates them to generate component surfaces with different scales. The procedure is as follows:

Step 1: Set the target surface $Z(x, y)$ as the initial working surface and apply the 2D-DTCWT to it at level J. Obtain the approximation coefficient a and detail coefficients d_j for $j = 1, 2, \ldots, J$.

Step 2: Reconstruct the approximate surface $Z_a(x, y)$ from a, and reconstruct each detail surface $Z_{d_j}(x, y)$ from d_j.

Step 3: Extract the non-negative portion of each detail surface $Z_{d_j}(x, y)$, yielding the positive detail surface $ZP_{d_j}(x, y)$.

Optics EXPRESS

Step 4: Update the decomposed residual $ZR(x, y)$ for the current iteration and the surface $Z'(x, y)$ for the next iteration:

$$\begin{cases} ZR(x,y) = Z(x,y) - Z_a(x,y) - \sum_{j=1}^{J} ZP_{d_j}(x,y) \\ Z'(x,y) = Z(x,y) - \sum_{j=1}^{J} ZP_{d_j}(x,y) \end{cases} \tag{9}$$

Iterations will terminate when any of the following stopping criteria is met: (1) the decomposed residual Root Mean Square (RMS) is greater than the previous iteration; (2) the convergence efficiency—defined as the ratio of RMS values between successive iterations—falls below the threshold δ; (3) the decomposed residual RMS falls below a target tolerance ε. These stopping rules follow practical manufacturing logic: when the residual meets the design tolerance, further fabrication is unnecessary and the process terminates.

After iterative refinement, IWTSD produces a large-scale component surface $ZL(x, y)$, J small-scale component surfaces $ZS_j(x, y)$ for $j = 1, 2, \ldots, J$, and a decomposed residual surface $ZR(x, y)$, as expressed by

$$\begin{cases} ZL(x,y) = Z_a^{(k)}(x,y) \\ ZS_j(x,y) = \sum_{i=1}^{k} ZP_{d_j}^{(i)}(x,y), j = 1, 2, \ldots, J \\ ZR(x,y) = Z(x,y) - ZL(x,y) - \sum_{j=1}^{J} ZS_j(x,y) \end{cases} \tag{10}$$

Here, k is the final iteration index. $Z_a^{(k)}(x, y)$ denotes the approximation at iteration k, and $ZP_{d_j}^{(i)}(x, y)$ denotes the non-negative portion of the j-th detail surface at iteration i.

Theoretically, increasing the number of decomposition scales allows better scale separation and can improve fabrication efficiency by enabling more scale-specific corrections. However, decomposition level J is limited by the data matrix size. And excessive decomposition scales typically require more tool types, more frequent CNC program updates, and extra tool changes, each of which increases total runtime and may introduce cumulative errors [22]. Consequently, it is generally optimal to decompose the target surface into two or three scale-specific components.

To balance practicality and effectiveness, we decompose the target surface into three components in this study: (1) a non-negative large-scale surface $ZL(x, y)$; (2) a non-negative small-scale surface $ZS(x, y)$; and (3) the decomposed residual surface $ZR(x, y)$. For the construction of the small-scale surface, we reconstruct only one detail surface $Z_{\{d_{j_1},\ldots,d_{j_2}\}}(x, y)$ from the selected detail coefficients $d_{j_1}, \ldots, d_{j_2}$ (with $1 \le j_1 \le j_2 \le J$), rather than reconstructing every individual detail $Z_{d_j}(x, y)$ in Step 2. After k iterations, three component surfaces are given by

$$\begin{cases} ZL(x,y) = Z_a^{(k)}(x,y) \\ ZS(x,y) = \sum_{i=1}^{k} ZP_{\{d_{j_1},\ldots,d_{j_2}\}}^{(i)}(x,y), 1 \le j_1 \le j_2 \le J \\ ZR(x,y) = Z(x,y) - ZL(x,y) - ZS(x,y) \end{cases} \tag{11}$$

where $ZP_{\{d_{j_1},\ldots,d_{j_2}\}}^{(i)}(x, y)$ denotes the non-negative portion of the reconstructed detail surface at iteration i. Algorithm 1 summarizes the IWTSD implementation.

2.3. Non-rectangle surface application and edge-decomposition ratio control

The 2D-DTCWT requires data on a rectangular grid. Hence, non-rectangular aperture surface data—such as the most common circular mirror surfaces—must be extended to an enclosing rectangular surface before decomposition. Surface extension methods fall broadly into frequency-domain and spatial-domain methods. Representative algorithms include the Gerchberg extension [28,29] and the Nearest-neighbors extension [30,31], both of which can rapidly produce a full rectangular mesh. The Nearest-neighbors extension fills missing mesh values and smooths the

Optics EXPRESS

Algorithm 1. Iterative wavelet-transform-based surface decomposition

Function IWTSD $(Z, J, \delta, \varepsilon)$**:**
  $k = 1, ZL = 0$;
  do
    $[a, d_1, d_2, \ldots, d_J] \leftarrow \mathrm{DTCWT}(Z)$;
    $Z_a \leftarrow \mathrm{IDTCWT}(a)$
    $Z_{\{d_{j_1},\cdots,d_{j_2}\}} \leftarrow \mathrm{IDTCWT}(d_{j_1}, \cdots, d_{j_2})$
    $ZP_{\{d_{j_1},\cdots,d_{j_2}\}} \leftarrow Z_{\{d_{j_1},\cdots,d_{j_2}\}}(Z_{\{d_{j_1},\cdots,d_{j_2}\}} > 0)$
    $ZS \leftarrow ZS + ZP_{\{d_{j_1},\cdots,d_{j_2}\}}$
    $ZR = Z - Z_a - ZP_{\{d_{j_1},\cdots,d_{j_2}\}}$
    if $\mathrm{RMS}(ZR) < \varepsilon$ **then**
      Break
    end
    $Z \leftarrow Z - ZP_{\{d_{j_1},\cdots,d_{j_2}\}}$
    $k \leftarrow k + 1$
  while $\mathrm{RMS}^k(ZR) < \mathrm{RMS}^{k-1}(ZR) \&\& (\mathrm{RMS}^k(ZR) - \mathrm{RMS}^{k-1}(ZR))/\mathrm{RMS}^{k-1}(ZR) > \delta$;
  $ZL \leftarrow Z_a$
  return ZL, ZS, ZR
end

boundary via local averaging while preserving the original edge height. Consequently, the turned up edge is primarily decomposed into the large-scale component surface, as shown in Fig. 2.

The height of the extension region substantially affects how edge errors are allocated between large-scale and small-scale components. To quantify this effect, we simulated a typical initial aspheric surface error plus a smaller-amplitude annular error, featuring a peak to valley (PV) value of 1 λ (λ=632.8 nm) and an RMS value of 0.2765 λ. Using the nearest-neighbors extension, we scale the extension height by a factor α to control the extended region's height and thus adjust the allocation of edge surface between the large-scale and small-scale surfaces, as shown in Fig. 3. For the test case, $\alpha = 0$ yields contributions of 49.66% (large scale) and 50.31% (small scale) to the target removal, whereas $\alpha = 1$ shifts the allocation to 92.56% (large scale) and 7.41% (small scale). For small α (e.g., $\alpha \approx 0.2$ in this example), the Nearest-neighbors and Gerchberg extensions produce comparable decompositions, and the turned-up edge is primarily decomposed into the small-scale component surface.

Figure 3(e) and 3(f) show that the RMS of the decomposed residual falls below 5% of the target surface RMS when α ranges from 0.4 to 0.8. In this range, the large-scale and small-scale surfaces account for about 80% and 20% of the target removal, respectively, enabling an effective balance between large-tool bulk correction and small-tool fine correction. Because edge-removal characteristics depend on the specific CCOS technologies and dwell time optimization methods, the optional extension factor α provides a flexible control parameter for combined fabrication across multiple tool sizes or different CCOS technologies. By selecting α according to the surface error distribution and the chosen technology's edge-removal characteristics, one can quickly set the extension height to control how edge errors are allocated between large-scale and small-scale surfaces.

In summary, the surface with multi-scale features can be decomposed into two or more non-negative, scale-specific component surfaces that require no additional non-negativity enforcement and can be used directly to calculate full-aperture dwell time. By choosing an appropriate surface extension method with an optimized extension factor, the allocation of edge errors can

Optics EXPRESS

be controlled. Following decomposition, polishing tools of suitable sizes are assigned to each scale-specific component surface to correct the corresponding errors, thus enabling efficient multi-tool fabrication of optical mirrors.

3. Simulation

To validate the effectiveness of the proposed IWTSD-based multi-tool fabrication method, this section will compare convergence efficiency and total dwell time for single-tool fabrication and multi-tool fabrication using several surface decomposition algorithms. All simulations were implemented in Matlab R2021b and executed on a standard personal computer equipped with an AMD Ryzen 7 5800H processor and 16 GB of RAM.

The target surface for simulation is sampled from a 1150 mm aperture mirror and has PV

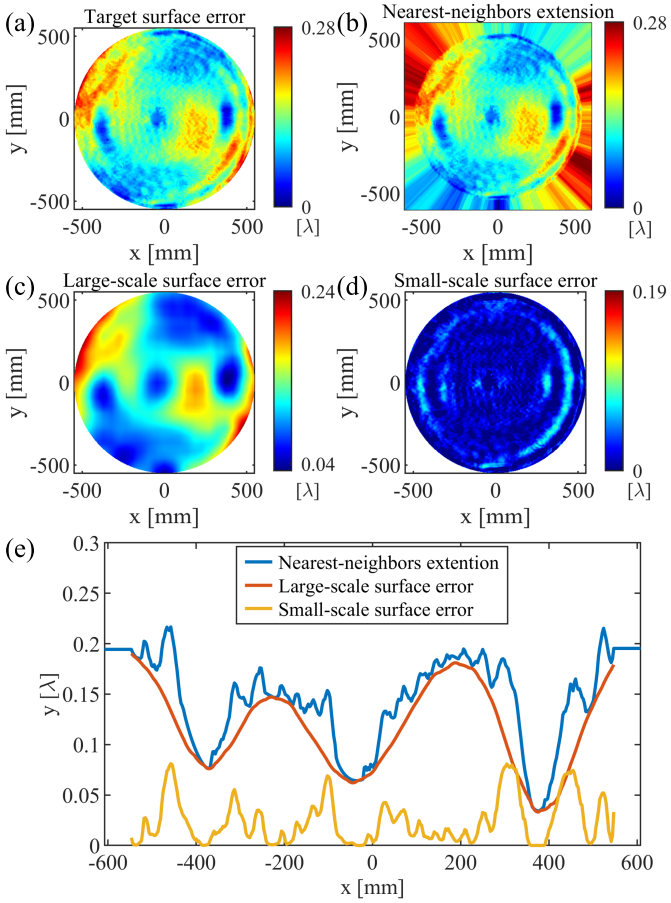

Fig. 2. IWTSD with Nearest-neighbors extension: (a) Target surface; (b) Surface after Nearest-neighbors extension; (c) Large-scale surface; (d) Small-scale surface; (e) Center profiles of surfaces.

and RMS values of 5.535 λ and 0.579 λ, respectively, as shown in Fig. 4(a). For the simulation of single-tool fabrication, we simulated polishing with a 200 mm diameter tool with a 30 mm orbital radius. The tool influence function (TIF1) is shown in Fig. 4(b). The full-aperture dwell time map was computed (Fig. 4(c)) by applying a space-invariant TIF in the inner region to reduce computational burden and a space-variant TIF at the edge region to improve edge error control accuracy. The detailed calculation procedure is described in our previous work [32]. The

Optics EXPRESS

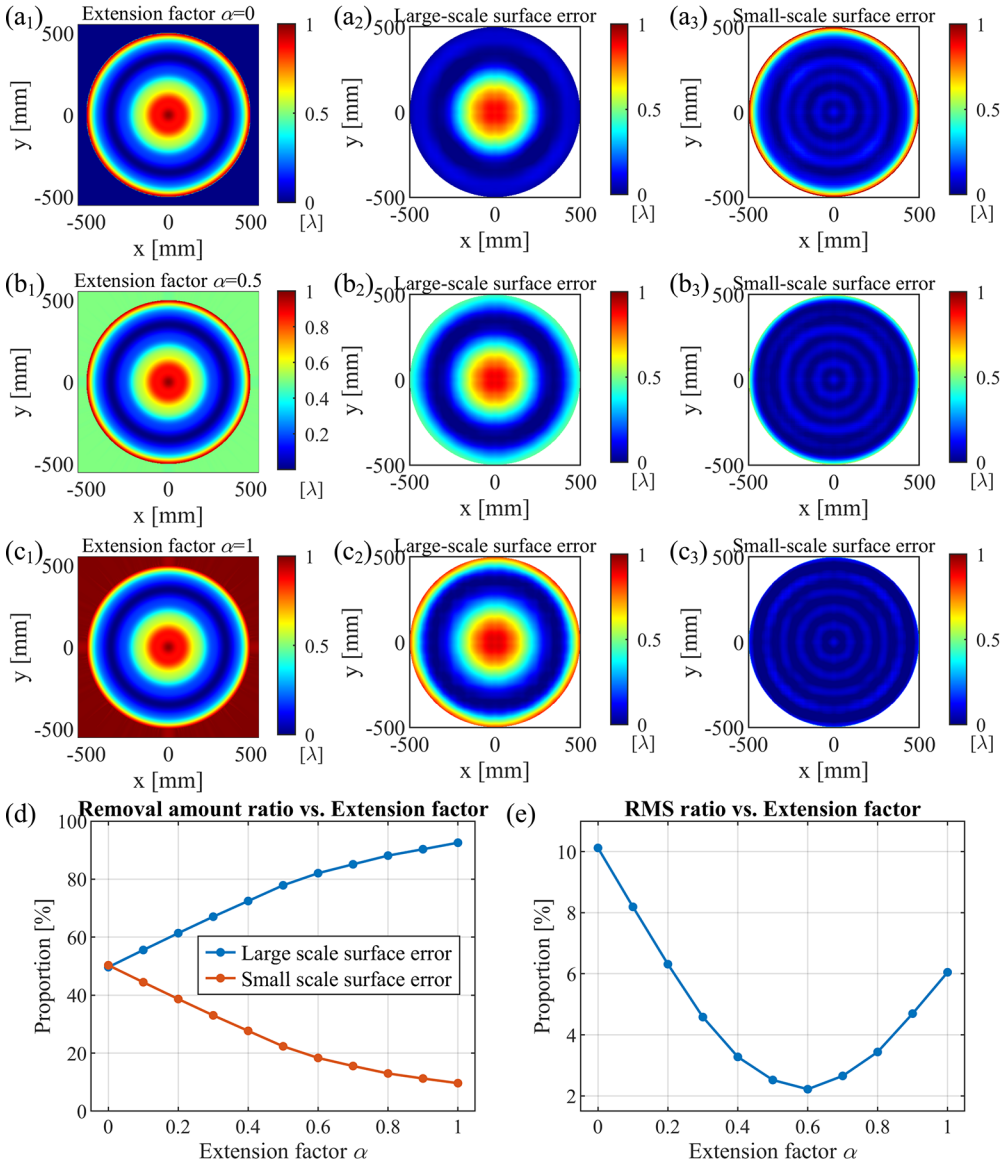

Fig. 3. Surface decomposition with different extension factor α. Extended surface, large-scale surface and small-scale surface with (a) α=0; (b) α=0.5; (c) α=1. All colorbars are uniformly set from 0 λ to 1 λ. (d) Removal amount ratio of large-scale and small-scale surface to the target surface; (e) RMS ratio of decomposed residual to the target surface.

simulated residual after polishing with TIF1 is given in Fig. 4(d). The total dwell time was 18.75 h, yielding residual PV and RMS values of 1.819 λ and 0.187 λ, corresponding to convergence efficiencies of 67.14% (PV) and 67.7% (RMS).

For the multi-tool fabrication, the target surface was decomposed by IWTSD into large-scale, small-scale, and residual surfaces. Prior to decomposition, we applied the Nearest-neighbors extension with extension factor α=0.6. Decomposing a 400 × 400 data grid required only 1.23 s on a personal computer, and the decomposition is presented in Fig. 5. Two polishing TIFs are selected for the multi-tool fabrication simulations: (1) TIF1 corresponding to a 200 mm tool with

Optics EXPRESS

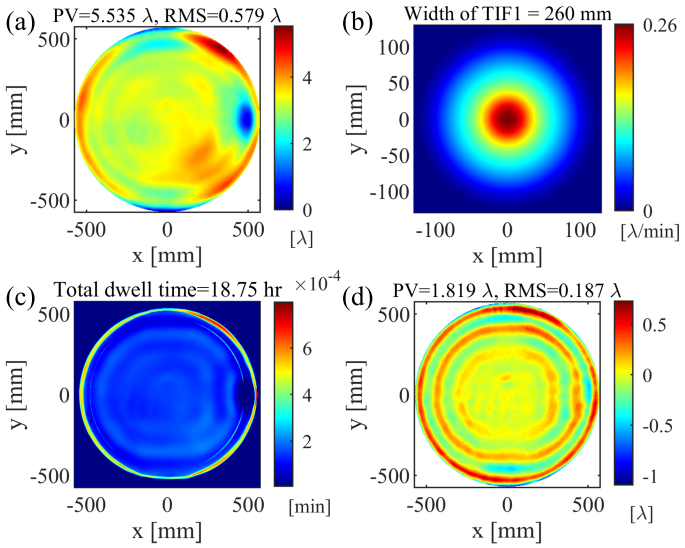

Fig. 4. Simulation of single-tool fabrication: (a) Target surface; (b) Tool influence function 1; (c) Dwell time; (d) Simulated residual.

30 mm orbital radius; and (2) TIF2 corresponding to a 100 mm tool with 15 mm orbital radius. Both TIFs have Gaussian-like profiles. Dwell times and simulated residuals were computed independently for the large-scale and small-scale surfaces. The overall residual was obtained by summing the residuals of the large-scale and small-scale surfaces and the decomposed residual. The total dwell time was 21.99 h (16.08 h for TIF1 and 5.91 h for TIF2), yielding residual PV and RMS values of 0.807 λ and 0.06 λ, corresponding to convergence efficiencies of 85.42% (PV) and 89.64% (RMS).

To compare the effects of different edge-surface decompositions on multi-tool fabrication, we repeated the decomposition using Gerchberg extension (decomposition time 3.29 s), as shown in Fig. 6. This extension tended to shift stiff roll-edge errors into the small-scale surface, producing a smoother decomposed residual. The resulting simulation (same TIFs as above) required a total dwell time of 21.93 h (16.38 h for TIF1, 5.55 h for TIF2) and produced residual PV = 0.883 λ and RMS = 0.056 λ, corresponding to convergence efficiencies of 84.05% (PV) and 90.33% (RMS). This result is close to that obtained by Nearest-neighbors extension with the extension factor $\alpha \approx 0.4$.

Additionally, we decomposed the target surface using Zernike polynomial fitting and frequency filtering to produce a large-scale component and a residual component, as shown in Fig. 7. We then computed the dwell time, simulated removal, and simulated residual for the large-scale component using TIF1. The small-scale component was obtained by subtracting the simulated removal from the target surface and enforcing non-negativity. Its dwell time and simulated residual were then computed using TIF2. Finally, the simulated residuals were obtained, as shown in Fig. 7(c) and 7(f). For multi-tool fabrication based on Zernike polynomial fitting, the total dwell time was 33.54 h (18.70 h for TIF1 and 14.84 h for TIF2). These yielded residual PV and RMS values of 0.928 λ and 0.057 λ, with convergence efficiencies of 83.23% (PV) and 90.16% (RMS). For multi-tool fabrication based on frequency filtering, the total dwell time was 32.38 h (17.86 h for TIF1, 14.52 h for TIF2). These yielded residual PV and RMS values of 0.905 λ and 0.058 λ, with convergence efficiencies of 83.65% (PV) and 89.98% (RMS). In these two methods, enforcing non-negativity on the small-scale component substantially increased total dwell time relative to IWTSD-based multi-tool fabrication.

Optics EXPRESS

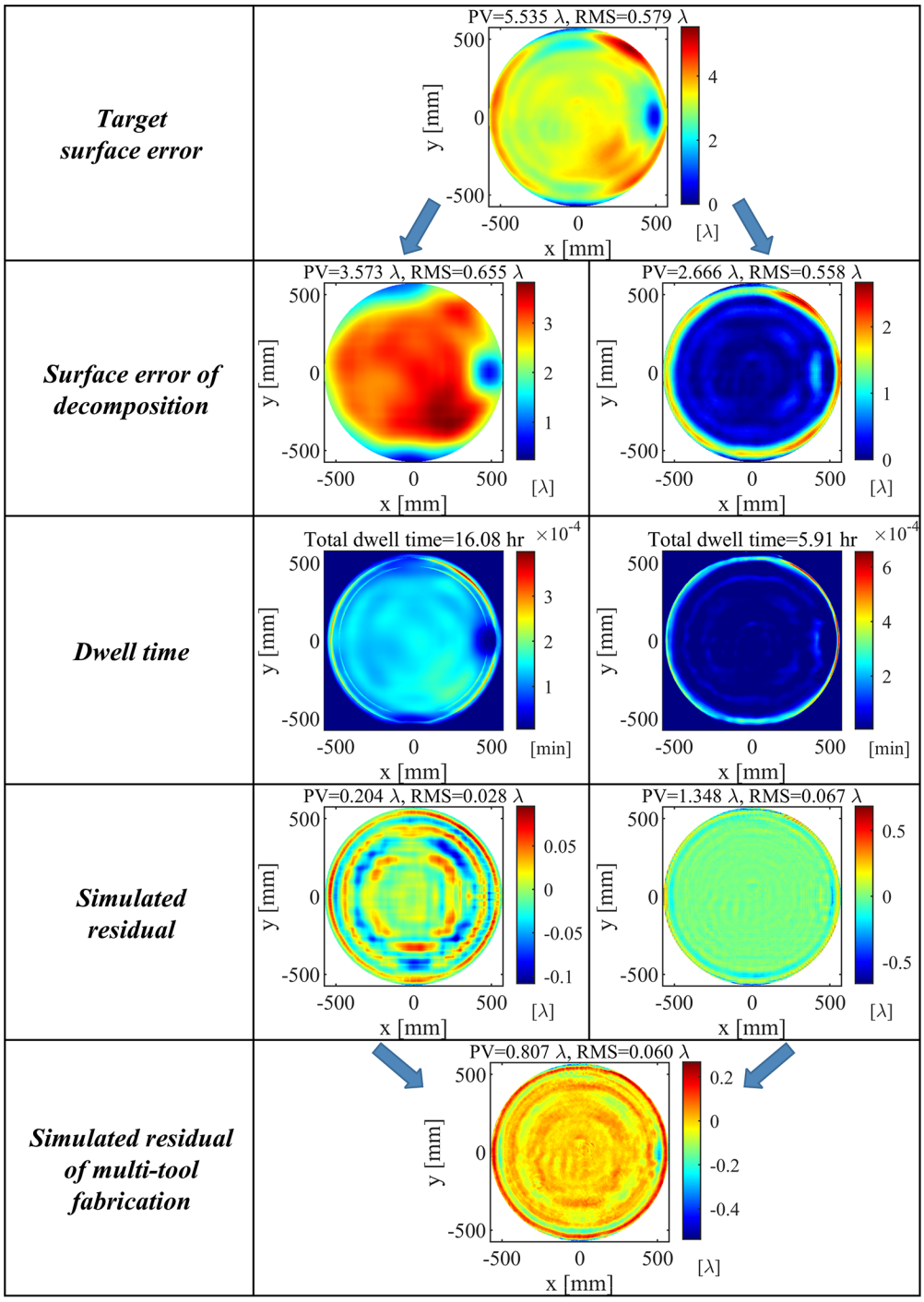

Fig. 5. Simulation of multi-tool fabrication using IWTSD with Nearest-neighbors extension.

Optics EXPRESS

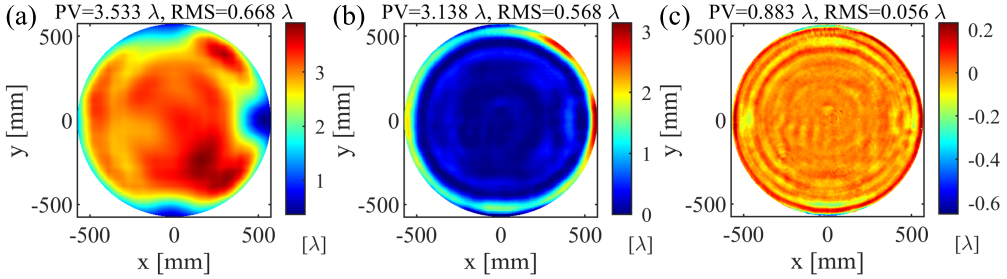

Fig. 6. Simulation of multi-tool fabrication using IWTSD with Gerchberg extension: (a) large-scale surface; (b) small-scale surface; (c) simulated residual of multi-tool fabrication.

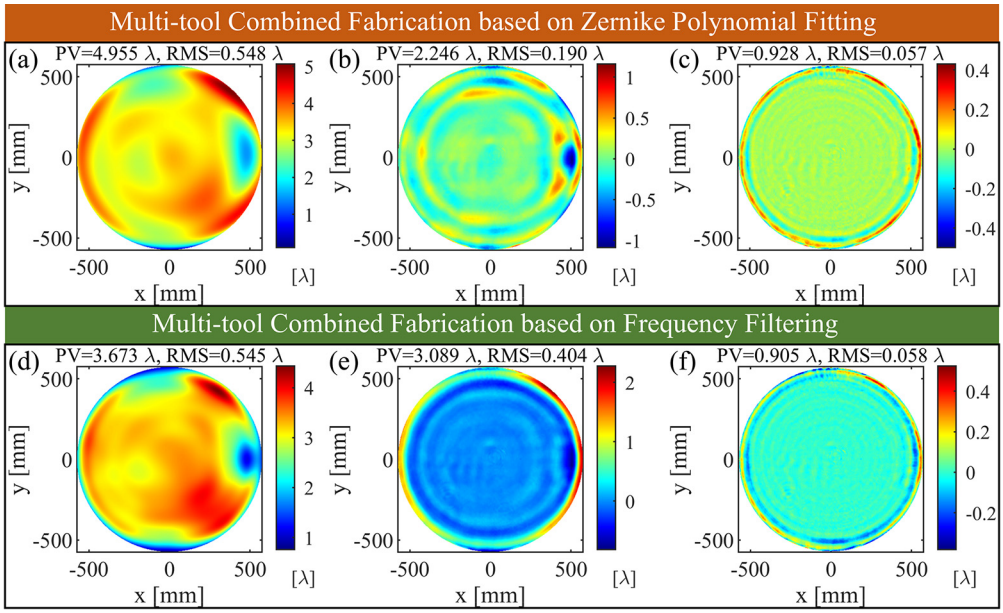

Fig. 7. Simulation of multi-tool fabrication using Zernike polynomial fitting: (a) large-scale surface; (b) small-scale surface; (c) simulated residual; Simulation of multi-tool fabrication using frequency filtering: (d) large-scale surface; (e) small-scale surface; (f) simulated residual.

Table 1 summarizes single-tool fabrication and multi-tool fabrication results obtained with various surface decomposition algorithms. Overall, multi-tool fabrication consistently outperforms single-tool fabrication: multi-tool fabrication reduced the residual RMS to roughly 1/3 of the single-tool fabrication residual. Moreover, multi-tool fabrication effectively removed the small-scale errors observed in the residual of single-tool fabrication. Compared with other multi-tool fabrication implementations, IWTSD-based multi-tool fabrication achieved higher convergence at total dwell times comparable to single-tool fabrication, and it required only about 66.63% of the total dwell time of other multi-tool fabrication approaches to reach similar accuracy, thereby improving both fabrication efficiency and final accuracy. Because our simulations use a full-aperture mirror polishing method that suppresses edge effects, the choice of extension methods had a negligible impact on total dwell time and convergence in IWTSD-based multi-tool fabrication. These indicate that IWTSD is compatible with common extension methods under the edge effect suppression strategy. In practice, however, the extension method and the

Optics EXPRESS

extension factor α should be selected with regard to the specific CCOS technology and the tools' edge-removal characteristics to achieve the desired balance between fabrication efficiency and accuracy. Additionally, appropriate selection of tool sizes presents a clear trade-off: smaller tools reduce residual error but increase total dwell time, whereas larger tools shorten dwell time at the expense of higher residuals. We simulated IWTSD-based multi-tool fabrication for different tool size combinations (Fig. 8). Simulation results indicate that the fastest convergence for the target surface in Fig. 4(a) would be achieved with a 350 mm tool for large-scale error correction and a 125 mm tool for small-scale error correction. However, since the curvature radius of polishing tools used in this paper is fixed, the tool diameter is restricted to no more than 200 mm for the off-axis aspheric mirror polishing here. Accordingly, the 200 mm and 100 mm tools selected in the simulation and subsequent experiment provide a favorable balance between dwell time and residual error. If technologies such as stressed-lap polishing are employed to correct large-scale errors, it could further improve convergence efficiency.

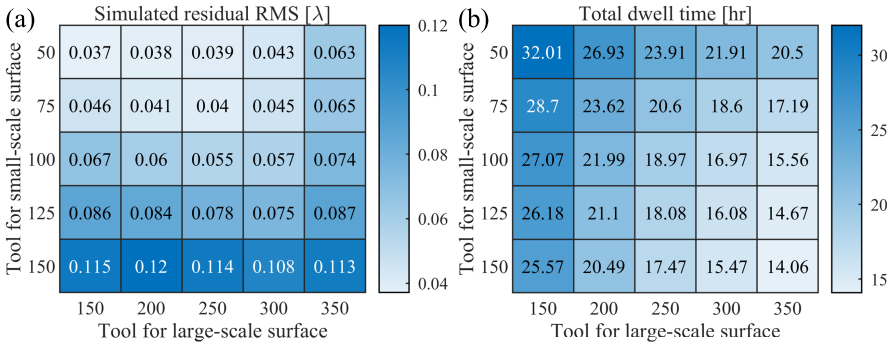

Fig. 8. (a) Simulated residual RMS; (b) Total dwell time for multi-tool fabrication under different tool size combinations.

4. Experiment

To validate the feasibility and reliability of the IWTSD and the associated multi-tool fabrication method, we performed polishing experiments on a 1150 mm off-axis aspheric mirror made of glass-ceramics. The workpiece is one segment of the stitched 4.4 m primary mirror of the Jiao Tong University Spectroscopic Telescope (JUST) [33]. The experimental mirror polishing setup is shown in Fig. 9(a). Workpiece parameters and polishing conditions are listed in Tables 2 and 3. Full-aperture measurements were performed with an interferometer and a computer-generated hologram (CGH), as shown in Fig. 9(b).

Table 1. Simulation results of single-tool fabrication and multi-tool fabrication obtained with various surface decomposition algorithms

Fabrication method	Total dwell time [hr]	Residual PV [λ]	Residual RMS [λ]	RMS convergence efficiency [%]
Single Tool	18.75	1.819	0.187	67.7
IWTSD with Nearest-neighbors	21.99	0.807	0.06	89.64
IWTSD with Gerchberg	21.93	0.883	0.056	90.33
Zernike polynomial fitting	33.54	0.928	0.057	90.16
Frequency filtering	32.38	0.905	0.058	89.98

The initial surface error and the surface error after each polishing round are shown in Fig. 10. In each round of dwell time calculation, IWTSD-based multi-tool fabrication consistently

Optics EXPRESS

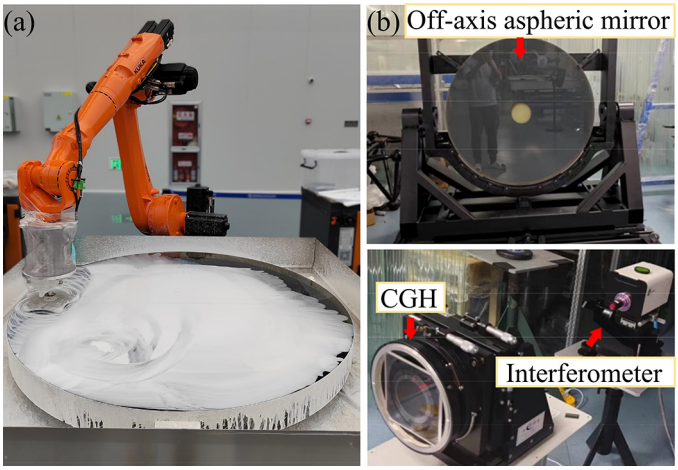

Fig. 9. (a) Experimental mirror polishing setup; (b) Optical path of the interferometric measurement using CGH.

Table 2. Detailed parameters of the workpiece

Diameter	1150 mm
Vertex radius of curvature	12800 mm
Conic Constant	−1.043 mm
Off-axis Distance	1652.815 mm
Concave / Convex	Concave
Material	Glass-ceramics

Table 3. Detailed working conditions of the polishing experiments

Tool diameter	200 mm, 100 mm
Tool radius of curvature	12800 mm
Spin velocity	150 rpm
Orbital velocity	−40 rpm
Orbital radius	0-30 mm, 0-15 mm
Pressure	40 N
Slurry	CeO_2
Polishing path	Raster

produced shorter total dwell time than alternative surface decomposition algorithms while maintaining comparable simulated residual error. Taking the initial surface error as an example, the IWTSD-based multi-tool fabrication required 8.04 h of polishing. It yielded simulated residuals of PV = 0.523 λ and RMS = 0.043 λ, compared with single-tool fabrication, which required 6.49 h but left a simulated residual of PV = 1.004 λ and RMS = 0.107 λ. Against other decomposition-based multi-tool fabrication, IWTSD required less fabrication time: Zernike polynomial fitting, 14.64 h (Residual PV = 0.55 λ, RMS = 0.042 λ); frequency filtering, 10.45 h (residual PV = 0.507 λ, RMS = 0.043 λ). For each polishing round, we recorded polishing time, overall PV and RMS, and PV/RMS for the large-scale and small-scale surfaces to evaluate polishing efficiency, as shown in Fig. 11. Both scale surfaces converged concurrently during polishing. The large-scale PV decreased from 2.93 λ to 1.151 λ and its RMS from 0.584 λ to

Optics EXPRESS

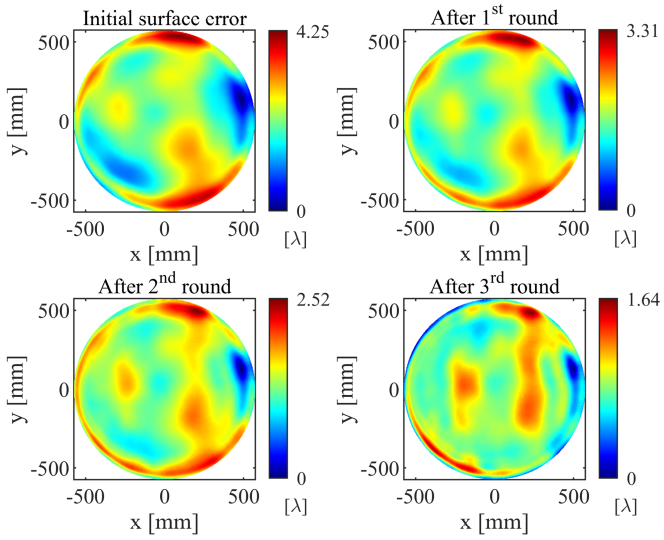

Fig. 10. Surface error maps in the iterative polishing using IWTSD-based multi-tool fabrication method

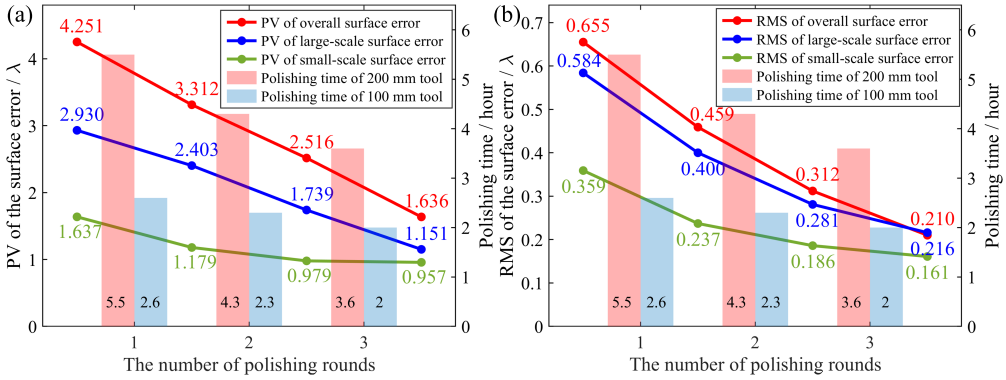

Fig. 11. (a) PV and (b) RMS of the surface error and polishing time in Fig. 10.

0.216 λ. The small-scale PV decreased from 1.637 λ to 0.957 λ, and its RMS from 0.359 λ to 0.161 λ. Overall surface RMS decreased rapidly—approximately 30% per round—reflecting concurrent multi-scale convergence. In the third round, the overall RMS convergence efficiency remained 32.69%, although the large/small scale RMS convergence dropped to 23.13%/13.44%. The relatively larger RMS values of the two scales are introduced by the non-negative calculation of our method, but it does not affect the convergence efficiency of the overall surface error. Because the small-scale surface from IWTSD does not require positive bias enforcement, three polishing rounds required only 20.19 h. Over these rounds, the overall PV decreased from 4.251 λ to 1.636 λ (61.51% reduction), and the overall RMS decreased from 0.655 λ to 0.21 λ (67.94% reduction). At this point, the surface error meets the acceptance criteria for the subsequent polishing stage. These experimental results demonstrate that the IWTSD and IWTSD-based multi-tool fabrication method substantially reduce total dwell time while improving fabrication efficiency for large-aperture mirrors.

Optics EXPRESS

5. Conclusion

Previous multi-tool fabrication approaches have been constrained by either high computation cost or extra fabrication time. To address these shortcomings, we propose an iterative wavelet-transform-based surface decomposition algorithm (IWTSD) and an associated multi-tool fabrication strategy. IWTSD applies the 2D-DTCWT with iterative refinement to produce accurate, non-negative, scale-separated component surfaces that can be used directly to compute full-aperture dwell time. A tunable surface extension procedure enables application of the 2D-DTCWT to non-rectangular apertures and provides control of edge component ratio for different scales.

Simulations and polishing experiments on a 1150 mm off-axis aspheric mirror demonstrate that the proposed IWTSD and its multi-tool fabrication strategy deliver substantial gains in both computational and fabrication efficiency. Simulations show that at dwell times comparable to single-tool fabrication, IWTSD-based multi-tool fabrication achieves significantly lower residual RMS. Conversely, to reach the same final surface accuracy as other multi-tool approaches, IWTSD requires only about two-thirds of their total dwell time. Experimental polishing confirms that errors at multiple spatial scales converge concurrently during each polishing round, producing rapid overall surface improvement. Together, the simulations and experiments indicate that IWTSD and its multi-tool fabrication method are applicable to precision mirror fabrication using CCOS, and are not limited to the small-tool polishing technology. Further improvement in the smoothness of the extended surface and in the selection of polishing tool sizes can increase convergence efficiency across scales and reduce total runtime. So more advanced surface-extension algorithms and tool-selection strategies will be studied in the future.

Funding. National Key Research and Development Program of China (2023YFA1605602); National Key Scientific Instrument and Equipment Development Projects of China (11627804).

Disclosures. The authors declare no conflicts of interest.

Data Availability. Data underlying the results presented in this paper are not publicly available at this time but may be obtained from the authors upon reasonable request.

References

1. J. Angel, "Very large ground-based telescopes for optical and ir astronomy," Nature **295**(5851), 651–657 (1982).
2. Q.-F. Xing, G. Zhao, Z.-W. Liu, *et al.*, "A metal-poor star with abundances from a pair-instability supernova," Nature **618**(7966), 712–715 (2023).
3. A. McPherson, J. Spyromilio, M. Kissler-Patig, *et al.*, "E-elt update of project and effect of change to 39m design," in *Ground-based and Airborne Telescopes IV*, vol. 8444 (SPIE, 2012), pp. 501–509.
4. L. Stepp, "Thirty meter telescope project update," in *Ground-based and Airborne Telescopes IV*, vol. 8444 (SPIE, 2012), pp. 510–525.
5. R. Aspden, R. McDonough, and F. R. Nitchie Jr, "Computer assisted optical surfacing," Appl. Opt. **11**(12), 2739–2747 (1972).
6. R. Wagner and R. Shannon, "Fabrication of aspherics using a mathematical model for material removal," Appl. Opt. **13**(7), 1683–1689 (1974).
7. R. A. Jones and W. J. Rupp, "Rapid optical fabrication with ccos," in *Advanced optical manufacturing and testing*, vol. 1333 (SPIE, 1990), pp. 34–43.
8. D. W. Kim, S.-W. Kim, and J. H. Burge, "Non-sequential optimization technique for a computer controlled optical surfacing process using multiple tool influence functions," Opt. Express **17**(24), 21850–21866 (2009).
9. S. West, R. Angel, B. Cuerden, *et al.*, "Development and results for stressed-lap polishing of large telescope mirrors1," in *Optical Fabrication and Testing*, (Optica Publishing Group, 2014), pp. OTh2B–4.
10. G. Yu, D. D. Walker, and H. Li, "Research on fabrication of mirror segments for e-elt," in *6th International Symposium on Advanced Optical Manufacturing and Testing Technologies: Advanced Optical Manufacturing Technologies*, vol. 8416 (SPIE, 2012), pp. 19–24.
11. T. Wang, L. Huang, H. Kang, *et al.*, "Rifta: A robust iterative fourier transform-based dwell time algorithm for ultra-precision ion beam figuring of synchrotron mirrors," Sci. Rep. **10**(1), 8135 (2020).
12. X. Ke, T. Wang, H. Choi, *et al.*, "Dual-tool multiplexing model of parallel computer controlled optical surfacing," Opt. Lett. **45**(23), 6426–6429 (2020).
13. K. Xu, H. Hu, X. Zhang, *et al.*, "Accuracy verification methodology for computer-generated hologram used for testing a 3.5-meter mirror based on an equivalent element," Light: Adv. Manufact. **5**(2), 1 (2024).

Optics EXPRESS

14. M. Li, Z. Wang, T. Lv, *et al.*, "High-precision measurement and control of geometric parameters of off-axis aspheric surface," in *AOPC 2023: Optical Design and Manufacturing*, vol. 12964 (SPIE, 2023), pp. 24–29.
15. H. Kang, T. Wang, H. Choi, *et al.*, "Genetic algorithm-powered non-sequential dwell time optimization for large optics fabrication," Opt. Express **30**(10), 16442–16458 (2022).
16. X. Ke, T. Wang, Z. Zhang, *et al.*, "Multi-tool optimization for computer controlled optical surfacing," Opt. Express **30**(10), 16957–16972 (2022).
17. Z.-Y. Liu, L.-X. Li, X.-F. Zeng, *et al.*, "Fabrication of large aspheric mirror using multi-mode polishing based on error separation," Opt. Precision Eng. **25**, 281–288 (2017).
18. X. Zhang, H. Hu, X. Wang, *et al.*, "Challenges and strategies in high-accuracy manufacturing of the world's largest sic aspheric mirror," Light: Sci. Appl. **11**(1), 310 (2022).
19. Z. Liu, L. Li, E. Qi, *et al.*, "Fabrication of a 4 m sic aspheric mirror using an optimized strategy of dividing an error map," Photonics **11**(2), 125 (2024).
20. H. Du, C. Song, S. Li, *et al.*, "Multi-tool selection model for the error control of mid-to-high frequency and rapid fabrication on large-scale aspheric optics," Optik **216**, 164635 (2020).
21. M. Xu, Y. Dai, X. Xie, *et al.*, "Fabrication of continuous phase plates with small structures based on recursive frequency filtered ion beam figuring," Opt. Express **25**(10), 10765–10778 (2017).
22. B. Zhong, W. Deng, X. Chen, *et al.*, "Frequency division combined machining method to improve polishing efficiency of continuous phase plate by bonnet polishing," Opt. Express **29**(2), 1597–1612 (2021).
23. Z. Yang, Y. Dai, and G. Wang, "Use of wavelet in specifying optics," Chin. Opt. Lett. **5**, 44–46 (2007).
24. K. Gröchenig, *Foundations of time-frequency analysis* (Springer Science & Business Media, 2001).
25. N. Kingsbury, "The dual-tree complex wavelet transform: a new efficient tool for image restoration and enhancement," in *9th European Signal Processing Conference (EUSIPCO 1998)*, (IEEE, 1998), pp. 1–4.
26. N. Kingsbury, "Complex wavelets for shift invariant analysis and filtering of signals," Appl. Computational Harmonic Analy. **10**(3), 234–253 (2001).
27. I. W. Selesnick, R. G. Baraniuk, and N. C. Kingsbury, "The dual-tree complex wavelet transform," IEEE Signal Process. Mag. **22**(6), 123–151 (2005).
28. R. Gerchberg, "Super-resolution through error energy reduction," Opt. Acta: International J. Opt. **21**(9), 709–720 (1974).
29. R. J. Marks, "Gerchberg's extrapolation algorithm in two dimensions," Appl. Opt. **20**(10), 1815–1820 (1981).
30. L. Zhou, Y. Dai, X. Xie, *et al.*, "Methods to extend surface error map in dwell time algorithm," in *EUSPEN's 16th International Conference & Exhibition*, (2016).
31. Y. Liu, H. Cheng, Z. Dong, *et al.*, "Edge effect of optical surfacing process with different data extension algorithms," Front. Optoelectron. **7**(1), 77–83 (2014).
32. J. Zhou, B. Li, and X. Li, "Efficient full-aperture mirror polishing method with variable orbital radius in computer-controlled optical surfacing," Opt. Express **32**(13), 23865–23881 (2024).
33. J. Team, C. Liu, Y. Zu, *et al.*, "The jiao tong university spectroscopic telescope project," Astron. Tech. Instruments **1**(1), 16–30 (2024).